



HAL
open science

Comparing the spatial and kinematic distribution of gas and young stars around the shell-like structure in the CMa OB1 association

J. Gregorio-Hetem, B. Lefloch, A. Hetem, T. Montmerle, B. Fernandes, E F Mendoza, M. de Simone

► To cite this version:

J. Gregorio-Hetem, B. Lefloch, A. Hetem, T. Montmerle, B. Fernandes, et al.. Comparing the spatial and kinematic distribution of gas and young stars around the shell-like structure in the CMa OB1 association. *Astronomy and Astrophysics - A&A*, 2021, 654, pp.A150. 10.1051/0004-6361/202141535 . hal-03796882

HAL Id: hal-03796882

<https://cnrs.hal.science/hal-03796882>

Submitted on 4 Oct 2022

HAL is a multi-disciplinary open access archive for the deposit and dissemination of scientific research documents, whether they are published or not. The documents may come from teaching and research institutions in France or abroad, or from public or private research centers.

L'archive ouverte pluridisciplinaire **HAL**, est destinée au dépôt et à la diffusion de documents scientifiques de niveau recherche, publiés ou non, émanant des établissements d'enseignement et de recherche français ou étrangers, des laboratoires publics ou privés.

Comparing the spatial and kinematic distribution of gas and young stars around the shell-like structure in the CMa OB1 association[★]

J. Gregorio-Hetem¹ , B. Lefloch² , A. Hetem³ , T. Montmerle⁴, B. Fernandes¹,
E. F. Mendoza^{1,5}, and M. De Simone^{2,6} 

¹ Universidade de São Paulo, Instituto de Astronomia, Geofísica e Ciências Atmosféricas, 05508-090 São Paulo, Brazil
e-mail: gregorio-hetem@usp.br

² Univ. Grenoble Alpes, CNRS, IPAG, 38000 Grenoble, France

³ UFABC Federal University of ABC, Av. dos Estados, 5001, 09210-580 Santo André, SP, Brazil

⁴ Institut d'Astrophysique de Paris, 75014, Paris, France

⁵ Observatório do Valongo, UFRJ, 20080-090 Rio de Janeiro RJ, Brazil

⁶ INAF, Osservatorio Astrofisico di Arcetri, Largo E. Fermi 5, 50125 Firenze, Italy

Received 13 June 2021 / Accepted 16 August 2021

ABSTRACT

Context. The relationship between young stellar clusters and their respective parental molecular clouds remains an open issue. Recent inquiries consider the similarities between substructures of clouds and clusters and whether they are a coincidence or, rather, an indication of a physical relationship. To address these issues, we studied the CMa OB1/R1 region, which shows evidence of a complex star formation history.

Aims. We obtained molecular cloud mapping with the IRAM-30 metre telescope to reveal the physical conditions of an unexplored side of the CMa region with the aim of comparing the morphology of the clouds to the distribution of young stellar objects (YSOs). We also studied the cloud kinematics in pursuit of gradients and jet signatures that could trace different star formation scenarios.

Methods. The YSOs were selected on the basis of astrometric data from *Gaia* EDR3 that characterize the moving groups. The distance of 1099^{+25}_{-24} pc was obtained for the sample, based on the mean error-weighted parallax. Optical and near-infrared photometry was used to verify the evolutionary status and circumstellar characteristics of the YSOs.

Results. Among the selected candidates, we found 40 members associated with the cloud: 1 Class I, 11 Class II, and 28 Class III objects. Comparing the spatial distribution of the stellar population with the cores revealed by the ¹³CO map, we verified that peaks of emission coincide with the position of YSOs, confirming the association of these objects to their dense natal gas.

Conclusions. Our observations support the large-scale scenario of the CMa shell-like structure formation as a relic of successive supernova events.

Key words. stars: pre-main sequence – circumstellar matter – ISM: individual objects: CMa OB1 – ISM: clouds – ISM: kinematics and dynamics – infrared: stars

1. Introduction

It is clear that OB associations are ideal sites for testing our understanding of star formation and how this process is influenced by the feedback from massive stars. The interplay between supernova (SN) events and the star-forming molecular cloud is of key relevance to the star formation process, as shown in several examples from the literature. In particular, it has been proposed that SN are able to affect star formation negatively by suppressing the formation of new stars in their surroundings, as well as positively by triggering it (see review by [Hensler et al. 2011](#)). In the latter case, the expansion of SN remnant (SNR) shells can sweep up the surrounding gas up to the point of triggering sequential star formation (according to the “collect and collapse” model of [Elmegreen & Lada 1977](#)).

The extended HII region Sh 2-235, for instance, is an active star-forming region where star formation triggered by a SNR

appears to have occurred in two nebulae: S235A and S235B ([Kirsanova et al. 2014](#)). The young stars associated with both nebulae are ~ 0.3 Myr old, coinciding with the age of the SNR proposed by [Kang et al. \(2012\)](#). Another interesting example is W28 SNR ([Lefloch et al. 2008](#); [Vaupré et al. 2014](#)), whose interaction with nearby molecular clouds could have triggered the formation of nearby protostellar clusters in the Trifid nebula. In the case of the SNR IC443, however, despite the fact that many young stellar objects (YSOs) are found surrounding the SNR shell, the SNR proved to be too young as compared to the age of YSOs and could not have triggered their formation ([Xu et al. 2011](#)). Recent numerical simulations by [Dale et al. \(2015\)](#) have been able to reproduce triggering of star formation. However, when making comparisons with observations, the authors found that triggered star formation is much harder to infer since they could not discriminate triggered from non-triggered objects.

Star formation is, in any case, often found in the vicinity of SNRs; for instance, there are several SNRs associated with YSOs in the Large Magellanic Cloud (e.g. [Desai et al. 2010](#)), and it has long been suggested that supernovae have the ability to excite star formation in their surrounding regions. The arc-shaped

[★] The reduced datacubes obtained with IRAM-30 m are also available at the CDS via anonymous ftp to [cdsarc.u-strasbg.fr](ftp://cdsarc.u-strasbg.fr) (130.79.128.5) or via <http://cdsarc.u-strasbg.fr/viz-bin/cat/J/A+A/654/A150>

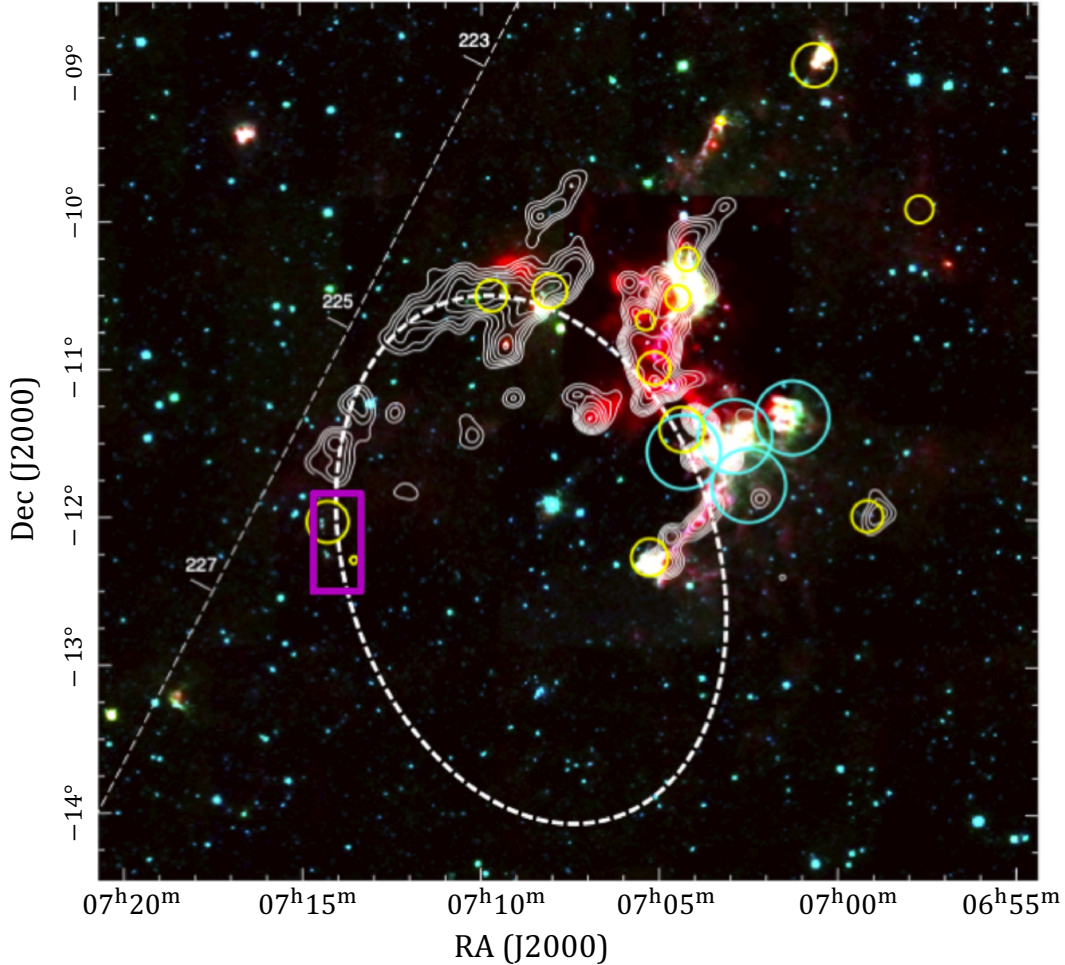


Fig. 1. Overview of the CMa R1 region. Background is a RGB composite WISE image (red: 22.2 μm , green: 12.1 μm , blue: 3.4 μm). The dashed straight line gives longitudes in the Galactic plane and the dashed ellipse shows the area of the CMa shell suggested by [Fernandes et al. \(2019\)](#). White contours trace the molecular gas (^{13}CO). X-ray observations with *XMM-Newton* ([Santos-Silva et al. 2018](#)) are indicated by cyan circles, and the groups of YSOs studied by [Fischer et al. \(2016\)](#) are shown as yellow circles. The area studied here is marked by the magenta box. The figure is adapted from [Fernandes et al. \(2019\)](#).

Sh 2-296 nebula is one of these cases, suspected to be an old SNR that might have triggered the formation of new stars in CMa OB1 ([Herbst & Assoua 1977](#)).

The Canis Major OB1/R1 (henceforth CMa, for simplicity) is a nearby ($d \sim 1$ kpc) OB Association with a complex star formation history. Our previous studies have shown that the region contains young objects originating from different star-forming events ([Gregorio-Hetem et al. 2009](#); [Santos-Silva et al. 2018](#)).

A promising hypothesis has been presented by [Fernandes et al. \(2019\)](#), demonstrating new evidence that Sh 2-296, the most prominent nebula in the CMa association, is part of a large (i.e., diameter of ~ 60 pc) shell-like structure. Figure 1 shows this structure, called the CMa “shell”, which is likely to have resulted from successive SN explosions from 6 to 1 Myr ago, as inferred from the past trajectories of three runaway stars in the region that were derived from *Gaia* proper motions. They also found evidence that the CMa shell is related to a larger (~ 140 pc in size) shell structure, visible in $\text{H}\alpha$. However, the older population of low-mass stars (>10 Myr), which are confirmed CMa members, cannot be explained by these recent SN explosions, suggesting that they may be causally related to the existence of the $\text{H}\alpha$ super-shell.

[Fernandes et al. \(2019\)](#) suggest that the present-day configuration of the star-forming gas may have been shaped by a

few successive SN explosions that occurred several Myr in the past. Despite the evidence of SN events shaping the CMa shell, [Fernandes et al. \(2019\)](#) argue that they probably played a minor role in triggering star formation in these clouds. Thus, CMa may serve an ideal laboratory for probing how the feedback from SNRs interacting with molecular clouds can affect their environment as well as the subsequent star formation and evolution in OB associations.

2. Molecular clouds in CMa

A ^{13}CO ($J = 1-0$) survey of [Kim et al. \(2004\)](#), using the Nagoya-4m telescope with a beam width of $2''.7$, identified 13 molecular clouds in the area of the CMa Association, distributed across three main structures around the clouds No. 3 ($l \sim 224^\circ$, $b \sim -2^\circ$), No. 4 ($l \sim 224.5^\circ$, $b \sim -1^\circ$), and No. 12 ($l \sim 226^\circ$, $b \sim -0.5^\circ$).

Partial maps of these molecular clouds were recently obtained with the 1.85 m mm-submm Telescope installed at the Nobeyama Radio Observatory¹. According to [Onishi et al. \(2013\)](#), the 1.85 m telescope is dedicated to a large-scale survey

¹ As courtesy of the Osaka Prefecture University group, a ^{13}CO map of the CMa region was obtained by T. Onishi & K. Tokuda (priv. comm.).

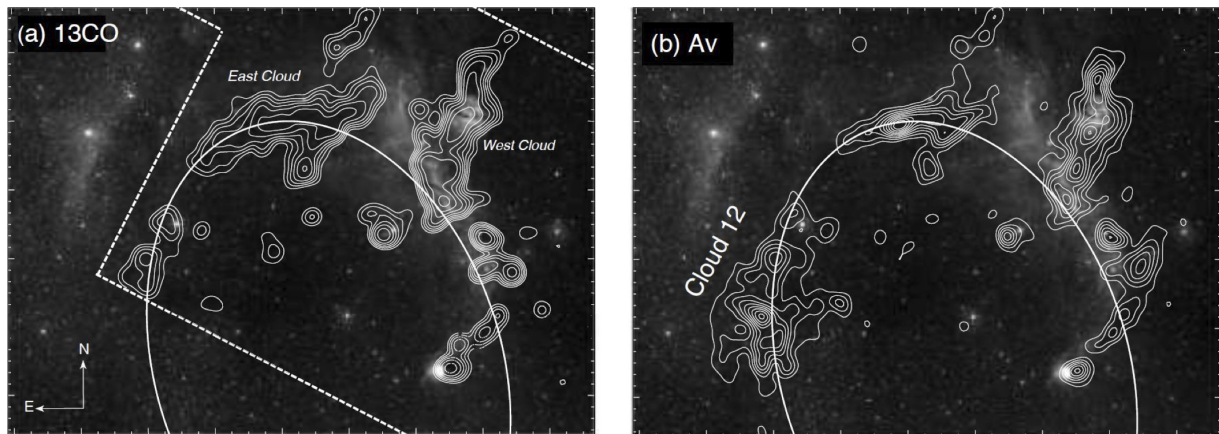


Fig. 2. DSS2-Red image of the Sh 2-296 nebula. The ellipse marks the proposed shape of the CMa shell and the contours in each panel trace: (a) the ^{13}CO emission (courtesy of the Osaka group, see Onishi et al. 2013); (b) extinction (A_V) from the 2MASS maps of Dobashi et al. (2011). The figure is adapted from Fernandes et al. (2019).

aiming to reveal the physical properties of molecular clouds in the Milky Way Galaxy. In the 1.3mm band, observations of the rotational transition $J=2-1$ of ^{12}CO , ^{13}CO and C^{18}O were obtained, with a beam size of $2'.7$.

The ^{13}CO map shows a chain of molecular clouds that extends north-east of the Sh 2-296 nebula. In Fig. 2a, the main structure associated with Sh 2-296 is referred to as the “west cloud”, which coincides with “Cloud 3” of the list from Kim et al. (2004). This is the largest cloud of the region, with a mass of $\sim 16000 M_{\odot}$ and an area of 358 pc^2 . To the north-east, the second main structure, called the “east cloud”, is related to “Cloud 4” (total mass $\sim 12000 M_{\odot}$ and area $\sim 301 \text{ pc}^2$).

The clouds are also traced by the dust distribution revealed by the extinction map of A_V (Fig. 2b) from Dobashi et al. (2011). We can see that the dust emission closely matches the ^{13}CO distribution, following the approximate shape of the CMa shell. Comparing Figs. 2a,b, we note that there is a lack of information on the ^{13}CO emission for “Cloud 12”, which is found in the area not covered in the survey obtained by the Osaka group (see the dashed rectangle in Fig. 2a). This cloud is the third-largest gas reservoir in the CMa association, with an estimated mass of $7500 M_{\odot}$ and an area of 315 pc^2 (Kim et al. 2004). Besides the significant amount of gas it holds, this cloud is located in the border of the CMa Shell, on the opposite side of Sh 2-296 nebula.

This work is dedicated to an investigation of this complementary area of gas distribution, which can bring an important contribution to the general understanding of the star formation scenario in CMa. In the general context, we aim to explore the global dynamics that allows us to search for signatures of the large-scale SNR-driven shock and its interaction with the molecular gas condensation. In Sect. 3, we summarize the surveys used in the analysis and the molecular gas observations. The identification and analysis of young stars associated with the cloud are presented in Sect. 4. Finally, in Sect. 5, we discuss the results from the molecular cloud mapping in comparison to the characteristics of the associated stellar population. The conclusions are summarized in Sect. 6.

3. Observational data

3.1. Dust continuum surveys

Besides the visual extinction map that is compared to the molecular cloud distribution in Sect. 2, here we analyze the dust distribution traced by the infrared emission. We are particularly

interested in the search for condensations and filamentary structures that is aimed at verifying whether they are harbouring pre- and protostellar cores, as suggested by Elia et al. (2013).

As part of the *Herschel* Infrared Galactic plane survey (HiGAL Molinari et al. 2010), Elia et al. (2013) conducted a study of star formation in the third Galactic quadrant, which includes the CMa region. In this study, *Herschel* PACS and SPIRE² photometric observations were combined with NANTEN CO $J=1-0$ observations of cores and clumps, revealing that most of the protostars are in the early accretion phase, while star formation is still underway in cores distributed along filaments.

The filamentary structure of “Cloud 12” studied here can be clearly seen in the *Herschel* SPIRE map obtained at $250 \mu\text{m}$, which is shown in Fig. 3 (left panel). The position of bright infrared sources (flux density $> 3 \text{ Jy}$ at $100 \mu\text{m}$ band) from the IRAS Catalogue of Point Sources (Helou & Walker 1988) is also plotted in this figure, showing a good correlation with the bright filaments.

We also performed the characterization of the infrared (IR) sources associated with the clouds by searching for candidates in the AllWISE catalogue (Cutri et al. 2013). The WISE photometry (Wright et al. 2010) at bands W1 ($3.4 \mu\text{m}$), W2 ($4.6 \mu\text{m}$), and W3 ($12 \mu\text{m}$) are useful for distinguishing among different classes of YSOs as a function of their IR excess.

As shown in Fig. 1, the CMa clouds contain several groups of YSO candidates identified by Fischer et al. (2016) based on WISE colors. The candidates were selected by adopting the criteria proposed by Koenig & Leisawitz (2014) to identify Class I and Class II objects. Details on this method, which we also apply here, is presented in Sect. 4.2.1. The distribution of the groups of YSOs found by Fischer et al. (2016) closely follows the border of the CMa Shell and coincides with the gas distribution.

3.2. Molecular gas

In order to characterize the properties of the cores and filaments associated with star formation activity, as revealed in the AllWISE and *Herschel* surveys, we used the IRAM-30 m telescope (Sierra Nevada, Spain) to map the emission of the ground-state

² Instruments on the *Herschel* Space Observatory (Pilbratt et al. 2010): PACS (Photodetector Array Camera & Spectrometer) (Griffin et al. 2010) covers the 70 and $160 \mu\text{m}$ bands, while SPIRE (Spectral and Photometric Imaging REceiver) (Poglitsch et al. 2010) operates at 250, 350, and $500 \mu\text{m}$.

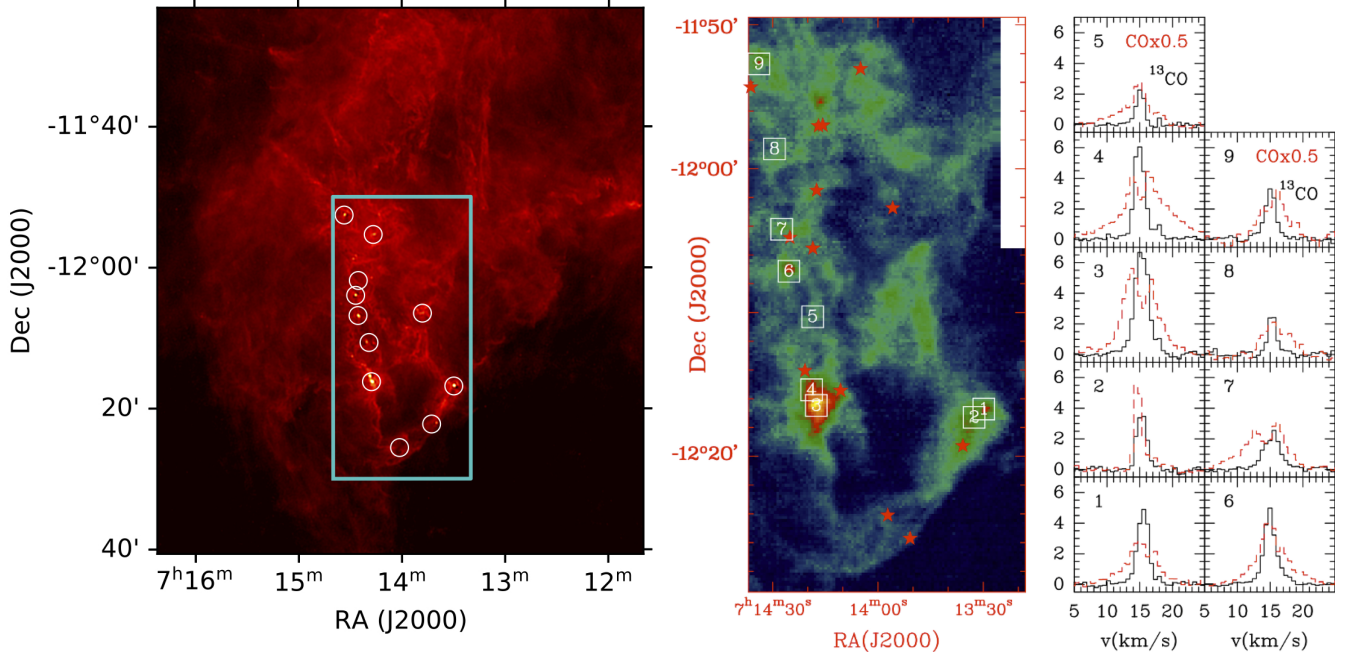


Fig. 3. Dust and gas observations. *Left:* region covered by the IRAM observations (cyan box) overlaid on the *Herschel* SPIRE 250 μm map that illustrates the filamentary structure of the cloud and the distribution of bright IRAS sources (white circles). *Middle:* ^{13}CO map revealing dense cores roughly related to the IRAS sources. The location of the WISE sources (Class I) are marked by red stars. The location of the nine dense cores listed in Table 1 is drawn with white squares. *Right:* core emission (T_{MB}) observed in the ^{13}CO (black) and ^{12}CO (dashed red) $J=1-0$ transitions. A scaling factor of 0.5 has been applied to the ^{12}CO line intensity.

Table 1. Observational properties of a sample of molecular cores.

Core	$\Delta\alpha$ (arcsec)	$\Delta\delta$ (arcsec)	RA (J2000) (^h ^m ^s)	Dec (J2000) ([°] ['] ^{''})	T_{kin} (K)	$N(^{13}\text{CO})$ (10^{16} cm^{-2})	$N(\text{H}_2)$ (10^{22} cm^{-2})	Outflow	Comment
1	-325	165	07 13 30	-12 16 43	8	3.3	2.1	Y	
2	-285	130	07 13 33	-12 17 18	8	3.3	2.1	N	
3	375	180	07 14 17	-12 16 28	13	5.0	3.3	Y	Broad wings
4	395	245	07 14 18	-12 15 23	13	3.5	2.3	Y	Broad wings
5	390	550	07 14 18	-12 10 18	10	3.8	2.5	Y	Broad wings
6	490	740	07 14 25	-12 07 08	12	1.2	0.8	Y	Small wings
7	520	915	07 14 27	-12 04 13	12	0.7	0.5	Y	Blueshifted wing
8	550	1250	07 14 29	-11 58 38	7	0.7	0.5	N	
9	615	1605	07 14 33	-11 52 43	9.5	1.2	0.8	N	

Notes. The physical parameters: kinetic temperature (T_{kin}), and column density ($N(^{13}\text{CO})$) were obtained from averaging the signal over a region of $20'' \times 20''$. A value $T_{\text{kin}} = 10$ K was adopted for Core 5 due to the lack of detection of C^{18}O .

rotational transition $J=1-0$ of CO and its rare ^{13}CO and C^{18}O isotopologues in Cloud 12. Observations were carried out during three observing runs in October 2018 (project 043-18), March 2019 (project 120-19), and October 2019 (project 034-20), using the EMIR receiver at 3 mm in its 2SB mode connected to the FTS spectrometer in its 192 kHz resolution mode. Observations were carried out using the “on-the-fly” mode. We chose a reference position, which we checked to be free of emission in the CO $J=1-0$ line. We mapped a total area of $20' \times 40'$ in the rotational transitions $J=1-0$ of CO, ^{13}CO and C^{18}O . Figure 3 (left panel) shows the mapped area superimposed upon an image of the continuum emission from Cloud 12 obtained by *Herschel* SPIRE at 250 μm (see Sect. 3.1).

The weather conditions were good and rather stable during the observing sessions. Atmospheric calibrations were performed every 12–15 min and showed the weather to be stable.

The pointing was monitored every hour on a nearby quasar and corrections were always found lower than $3''$. Special attention was paid to the line calibration and we obtained a very good agreement among the different runs. The calibration uncertainty is about 10% in the 3 mm band.

The data reduction was performed using the GILDAS software developed at IRAM³. The line intensities are expressed in units of antenna temperature corrected for atmospheric attenuation and rearward losses (T_{A}^*). For the subsequent radiative transfer analysis of the pre- and protostellar core emission, line fluxes were expressed in units of main beam temperature (T_{MB}). The main beam efficiency and the half power beam width (HPBW) were taken from the IRAM webpage⁴.

³ <http://www.iram.fr/IRAMFR/GILDAS/>

⁴ <http://publicwiki.iram.es/Iram30mEfficiencies>

Table 2. Limits used for the *Gaia* data query and results from the kinematic members selection.

ID	RA (J2000)	Dec (J2000)	ϖ (mas)	μ_α (mas yr ⁻¹)	μ_δ (mas yr ⁻¹)
Query range	07 ^h 13 ^m to 07 ^h 15 ^m	-12°35' to -11°45'	0.4 to 2	-7 to 1	-4 to 4
$P \geq 50\%$	07 ^h 13 ^m 7 to 07 ^h 14 ^m 4	-12°14' to -11°58'	0.87 ± 0.30	-3.26 ± 0.44	1.08 ± 0.46
CMa06	07 ^h 03 ^m 7 to 07 ^h 05 ^m 6	-11°34' to -11°00'	0.85 ± 0.09	-4.18 ± 0.36	1.52 ± 0.21
Sh 2-296	07 ^h 01 ^m 2 to 07 ^h 06 ^m 8	-12°12' to -10°48'	0.8 to 1.25	-4.10 ± 0.60	1.50 ± 0.40

Notes. Our sample ($P \geq 50\%$) is compared with clusters CMa06 (Santos-Silva et al. 2021) and Sh 2-296 (Gregorio-Hetem et al. 2021) located to the W direction of the CMa shell.

The right panel of Fig. 3 illustrates the pre- and protostellar condensations that were detected thanks to the IRAM-30 m angular resolution. Table 1 gives the results for a sample of molecular cores shown in Fig. 3 (middle panel).

4. Stellar population

Two groups of YSOs (Fischer et al. 2016) are projected onto the eastern border of the CMa shell, coinciding with the location of the “Cloud 12” identified by Kim et al. (2004). Our preliminary analysis on the distribution of YSO candidates (selected from the AllWISE catalogue) is well correlated with the dust distribution revealed by the A_V map in a 800 arcmin² area within the cloud (Fig. 2).

Here, we extracted optical and infrared data (public catalogues) for stars found in the direction of the fields observed with IRAM-30m, searching for candidates that are likely to be members associated with the cloud (Sect. 4.1). The selected members are then characterized on the basis of infrared colors that allow us to identify Classes I and II objects (Sect. 4.2.1). The confirmation of the pre-main sequence nature of the candidates is obtained from a color-magnitude diagram using *Gaia* EDR3 photometry (Sect. 4.2.2).

4.1. Selection of members

With the aim of excluding the presence of field-stars in the sample, as well as confirming the membership of the objects associated with the cloud, we performed a selection of kinematic members by using the techniques described by Hetem & Gregorio-Hetem (2019). Following the formalism presented by Dias et al. (2014), the adopted statistical methods use likelihood model and cross entropy technique to estimate the probability of a candidate to be (or not to be) considered a cluster member. A vector of parameters consisting of astrometric and kinematic data given by the observed proper motion is used to calculate the probability density function for a candidate and for the background of field-stars. The membership probability basically results from the fitting of a Gaussian in 5D phase space (three positions and two components of proper motion) by comparison with the Gaussian background. Since the cross entropy is sensitive to the initial parameters, a genetic algorithm code is adopted for parameters optimization (Hetem & Gregorio-Hetem 2019).

The first subset of candidates was obtained by querying astrometric and kinematic data from the *Gaia* EDR3 catalogue (Gaia Collaboration 2016b, 2020a). The search was performed in an area slightly larger than the fields observed with IRAM-30m. We also delimited the query in ranges of parallax and proper motion compatible with results previously found for CMa (e.g. Santos-Silva et al. 2021). According to the *Gaia* technical

recommendations⁵, we applied the RUWE⁶ < 1.4 and $\varpi/\sigma_\varpi > 3$ selection filters in order to avoid any low quality with regard to the astrometric solution.

Table 2 gives the intervals of parameters adopted for the catalogue query, as well as the results found for our sample. The mean values obtained for proper motion define the membership criteria. An illustration of the reliability of the method is given in Fig. 4 (left panel), where the distribution of probabilities is presented as a function of a modulus of proper motion $|\mu| = [(\mu_\alpha)^2 + (\mu_\delta)^2]^{0.5}$. We suggest that objects with membership probability $P \geq 50\%$ are very likely associated with the ambient cloud, which are considered very likely CMa members here. These members have a value of (μ_α, μ_δ) that is within 1σ of the mean values found for the sample. Objects appearing below the dashed line ($P < 50\%$) in Fig. 4 (left panel) are considered candidates or probable field stars, since they have proper motion parameters in ranges that are larger than the 1σ threshold adopted by us.

Santos-Silva et al. (2021) use HDBScan technique to fit five parameters from *Gaia* aiming to explore the stellar clusters and sub-groups in the entire CMa region. No sub-group was found by them in the area studied here, probably due to the low number of members, or the objects are too faint to be identified by the automatic procedure. However, it is interesting to compare our results with those found by Santos-Silva et al. (2021) for the group they call “CMa06”, which coincides with the Sh 2-296 nebula (see the “west cloud” in Fig. 2a). Despite the fact that this cluster is located on the opposite side of the CMa shell ($\sim 2^\circ$ to the W), its parallax and proper motion are quite similar to the results of our sample. This may be due to a common star formation history. A similar result was independently achieved by Gregorio-Hetem et al. (2021) in the study of objects associated with Sh 2-296 using the same method adopted here (Hetem & Gregorio-Hetem 2019), which validates our criteria with regard to the selection of cloud members. The results found for CMa06 and Sh 2-296 are also presented in Table 2.

In order to evaluate the error-weighted parallax, we adopted the calculation used by Navarete et al. (2019), based on the uncertainty on the measured parallax (ϖ) and the spatial correlation between the position of the sources. We obtained for our sample the mean parallax ($\langle \pi \rangle = 0.91 \pm 0.02$ mas) that was converted to the distance of 1099^{+25}_{-24} pc. Figure 4 (right panel) shows the distribution of parallaxes and error bars given in Table A.1, highlighting 11 stars (2 Class II and 9 Class III) that coincide with the secondary structure of the cloud found in the centre of the gas distribution, as discussed in Sect. 5.

⁵ http://www.rssd.esa.int/doc_fetch.php?id=3757412

⁶ Re-Normalized unit weight error (see details in the technical note GAIA-C3-TN-LU-LL-124-01).

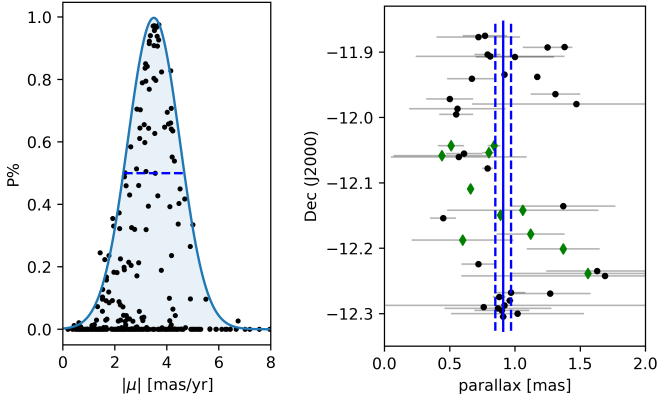


Fig. 4. Proper motion and parallax. *Left:* distribution of membership probabilities as a function of modulus of proper motion. A dashed line is used to separate members from candidates. *Right:* parallax distribution for the sample showing the observed values of ϖ and respective error bars. Green \blacklozenge symbols indicate the sources found in the secondary structure of the cloud (see Sect. 5). The vertical blue lines indicate the error-weighted mean parallax $\langle \varpi \rangle = 0.91 \pm 0.02$ mas (dashed lines show 3σ deviation).

4.2. Characterization

4.2.1. Infrared excess

The IR data from AllWISE catalogue were used for two purposes: (i) characterizing the stars that were selected as members of CMa on the basis of proper motion; and (ii) searching for embedded sources that were not detected by *Gaia*, likely due to high levels of extinction in dense regions. The query was restricted to the same area described in Sect. 4.1.

Our analysis of IR-excess is based on color-color diagrams using WISE bands: W1 (3.4 μ m), W2 (4.6 μ m), and W3 (12 μ m) that are useful to distinguish different classes of pre-main sequence stars. Based on the results from [Rebull et al. \(2014\)](#) for the Taurus star-forming region, [Koenig & Leisawitz \(2014\)](#) proposed limits on the $[W1-W2] \times [W2-W3]$ diagram defining the expected locus for Class I and Class II objects due to their significant IR-excess compared with Class III objects and field-stars.

In order to ensure the photometric quality, we extracted from the AllWISE catalogue only the sources that are in agreement with the following conditions for the magnitude measured at 12 μ m: $0.45 < W3_{r\chi^2} < 1.15$ and $W3_{snr} > 5$, where $r\chi^2$ and SNR correspond to the photometric error and signal-to-noise ratio (S/N), respectively. According to [Koenig & Leisawitz \(2014\)](#), these filters are applied with the purpose of mitigating any contamination from fake detections.

Figure 5 displays the $[W1-W2] \times [W2-W3]$ diagram for 383 sources that coincide with the fields observed with IRAM-30m and that are common on both catalogues: *Gaia* and WISE, which membership probability is represented by different symbols. It can be noted that most of the studied objects (89%) are plotted in the region where Class III or field-stars are expected to be found.

Our final sample contains 40 members (1 is Class I; 11 are Class II; and 28 are Class III) confirmed by proper motion ($P \geq 50\%$), and 4 candidates (1 is Class I, and 3 are Class II). Since we are mainly interested in embedded objects, Class III candidates ($P < 50\%$) were not included in the sample. Table A.1 gives the list of objects and the *Gaia* EDR3 parameters used in the membership probability calculation. The division

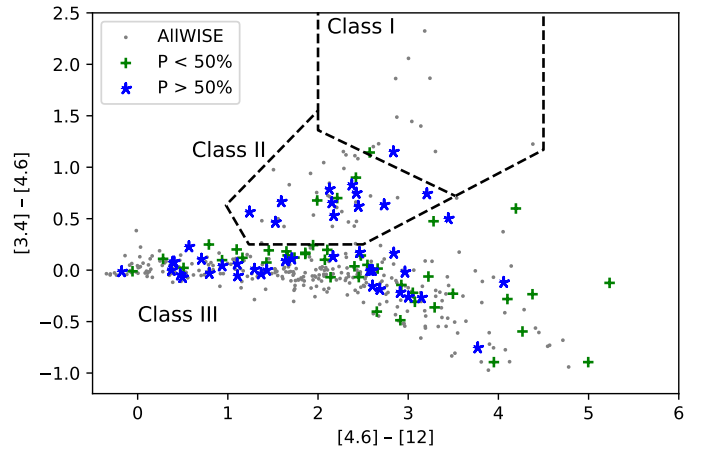


Fig. 5. WISE color-color diagram displaying the expected locus for Class I and Class II sources as proposed by [Koenig & Leisawitz \(2014\)](#). Confirmed members (blue \star) have $P \geq 50\%$, while possible members (green $+$) have $P < 50\%$. The remaining AllWISE objects (grey dots) are not present in the *Gaia* EDR3 catalogue. The IR sources found in the Classes I and II boxes are considered here as additional candidates.

between the classes of objects is indicated by double-lines in Table A.1.

With the aim of complementing the list of objects, we also searched for WISE sources that were not detected by *Gaia*. Due to the lack of membership information for these additional sources, only Class I or Class II objects are considered by us as possible members. In other words, among the WISE candidates not detected by *Gaia*, Class III objects were not taken into account due to the difficulty in distinguishing them from field stars. In this way, the sample is complemented by 45 WISE sources that we consider possible members (12 are Class I and 33 are Class II). The distribution of the sources in the equatorial coordinates space is shown in Fig. 6 (left panel). The IR photometry used in the analysis of the stellar population is given in Table A.2 for the same list presented in Table A.1.

For our sample, we verified the presence of $H\alpha$ emitters by using a cross-correlation with the results from [Pettersson & Reipurth \(2014\)](#) that revealed 353 new $H\alpha$ stars in the direction of CMa. The area surveyed by us contains ten $H\alpha$ stars. However, only four of them coincide with the CMa members, meaning that the other $H\alpha$ stars have proper motion or parallax in disagreement with the kinematic selection criteria adopted by us. In Table A.1, we added a comment marking each of the $H\alpha$ stars as identified by [Pettersson & Reipurth \(2014\)](#), which are classified by us as Class II objects. For classical T Tauri stars, the $H\alpha$ emission is an evidence of accretion process that is expected for Class II objects and is also related to the presence of a circumstellar disk. The characteristics of these four $H\alpha$ stars are in agreement with their young age (< 5 Myr), which is estimated in the next section.

4.2.2. Cluster age

In order to confirm the youth of the sample, we constructed a color-magnitude diagram using the photometric data at bands G (~ 600 nm), G_{BP} (~ 500 nm), and G_{RP} (~ 700 nm) from *Gaia* EDR3. The magnitudes were corrected for reddening by adopting the A_V/A_V relations from [Cardelli et al. \(1989\)](#). For each source, we calculated the distance modulus given by its parallax, which was used to estimate the unreddened absolute magnitude (M_G)₀.

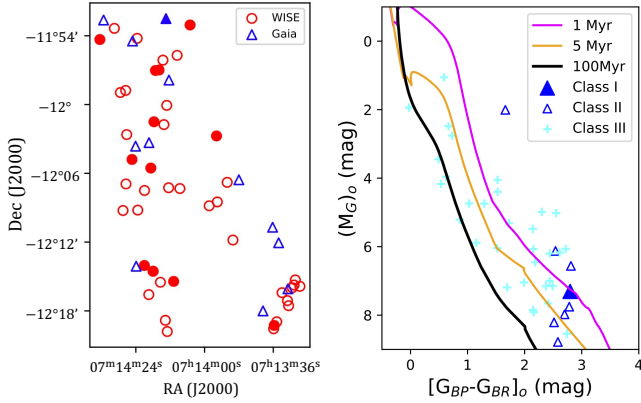


Fig. 6. Spatial distribution and color-magnitude diagram. *Left:* equatorial coordinates of Class I (filled symbols) and Class II (open symbols) that are CMA members (triangles) and additional candidates from All-WISE catalogue (circles). *Right:* absolute magnitude as a function of color from *Gaia* data for the CMA members ($P \geq 50\%$). The magnitudes are corrected for extinction. We use isochrones from PARSEC models, by adopting the 100 Myr line as representative of the ZAMS.

Figure 6 (right panel) shows the distribution of our sample in the $(M_G)_0 \times [G_{BP} - G_{RP}]_0$ diagram compared with isochrones from PARSEC⁷ (Bressan et al. 2012; Marigo et al. 2017). The models for 1 and 5 Myr were adopted to indicate the range of ages previously reported for the CMA young population (Gregorio-Hetem et al. 2009), while the 100 Myr isochrone was chosen as representative of the zero-age main sequence (ZAMS).

In the color-magnitude diagram, we display only the sources with good photometric data, which show $S/N > 10$ in all bands. Some of the Class III objects show a good fit with the ZAMS, indicating that we adopted a suitable mean value of visual extinction ($A_V = 0.9$ mag) in the reddening correction. Since the Class III objects are not affected by circumstellar IR-excess, we argue that this low level of A_V corresponds to the interstellar reddening in the direction of CMA, which is in agreement with the extinction map of the region (Gregorio-Hetem 2008). We conclude that it is highly probable that the Class III stars are observed in the near vicinity, but are preferentially located in the foreground of the cloud.

The same can be said for other sources detected by *Gaia*, since they are visible. However, some of them are too faint ($(M_G)_0 > 8$ mag in right panel of Fig. 6), probably due to a reddening that needs to be corrected with a higher value of A_V , which should be evaluated individually. This can be the case of sources that are still surrounded by some amount of cloud material.

We are aware that the use of optical color-magnitude diagrams gives only a rough estimation of age. Despite this, it can still be noted that most of the sources exhibiting IR excess (Class I and Class II) are ~ 5 Myr or younger. Several of the Class III presented here are in the same range of age and a few sources seem to be older, but still in the pre-main sequence phase, confirming the youth of our sample. Among the *Gaia* EDR3 sources, we do not find any massive stars. The brightest Class III objects have colors similar to those $2 M_\odot$ stars.

As mentioned in Sect. 4.1 the proper motion of our sample, which is located in the east side of the CMA shell, coincides with the values found for group CMA06 located to the west. The estimated age for this group is 6 ± 1 Myr (Santos-Silva et al. 2021),

⁷ Version v1.2S+COLIBRI PR16 of PARSEC models available on <http://stev.oapd.inaf.it/cgi-bin/cmd>

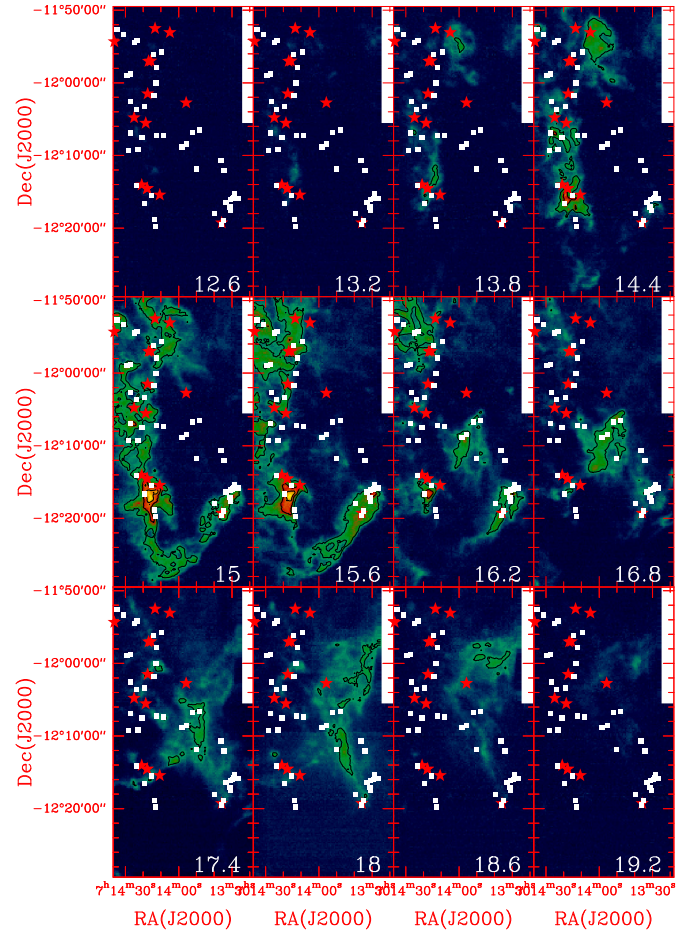


Fig. 7. Molecular gas mapping (^{13}CO) as a function of velocity given in km s^{-1} (see right bottom of each panel). The position of WISE sources is shown for Class I (red stars) and Class II (white squares) objects.

suggesting that these two stellar clusters, which are located at opposite sides, may have had a similar star formation scenario.

5. Comparing gas and star distributions

As can be seen in Figs. 3 and 6, the projected spatial distribution of our sample of stars closely follows the filamentary structure present in the ^{13}CO gas. Most of the Class II sources are found around dense cores, probably having emerged from the cloud and are still associated with it.

In Fig. 7, we plot a mosaic of ^{13}CO maps showing in each panel a different range of gas velocity, from 12.6 to 19.2 km s^{-1} . A main structure with $V = 15 \pm 1.2$ km s^{-1} is clearly seen at $\text{RA} \sim 07^{\text{h}} 14^{\text{m}} 5$, growing from N to S and then continuing to SW. A secondary structure at $V = 17.4 \pm 1.2$ km s^{-1} appears then at the centre of the plot ($\text{RA} = 07^{\text{h}} 14^{\text{m}}$, $\text{Dec} = 12^\circ 10'$). Despite their partial overlapping, they seem to be two structures representing different parts or movements of the cloud. The relative motions of these two gas structures are suggestive of a large-scale expanding gas motions around the cavity detected in the molecular gas at IRAM and in the continuum emission with SPIRE (see Fig. 3). It is remarkable that the “cavity” appears to be void of young stars and protostars.

The presence of these two cloud structures and their connection with the stellar population was confirmed by analyzing the gas kinematics through moment maps similar to the works by Álvarez-Gutiérrez et al. (2021) and Stutz & Gould (2016),

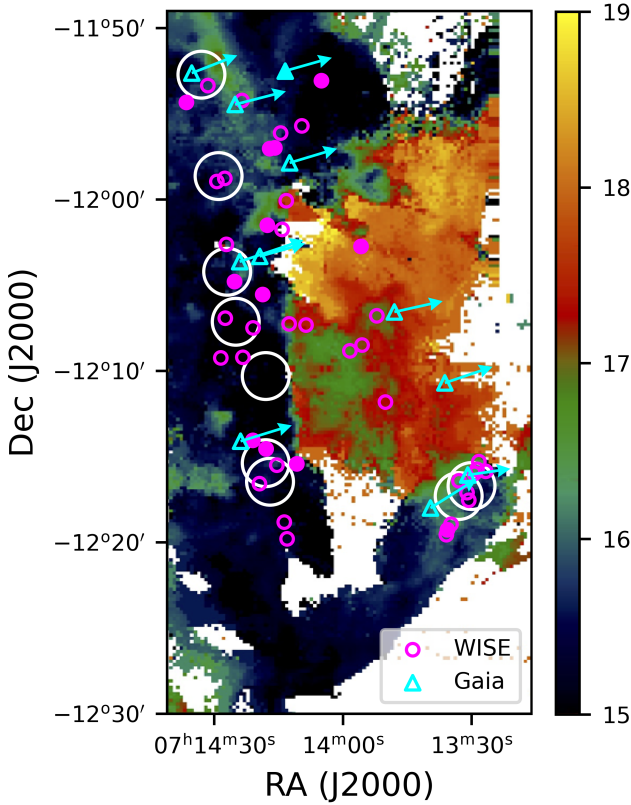


Fig. 8. Moment 1 map showing the distribution of velocities measured in km s^{-1} , based on ^{13}CO data. The proper motion vectors are displayed for the YSOs that are *Gaia* sources (same symbols as Fig. 6). White circles indicate the position of dense cores (see Fig. 3).

for instance. Based on the ^{13}CO observations, we obtained the moment 1 (mean velocities) map that is presented in Fig. 8 overlaid by the distribution of the YSOs that are Class I and Class II objects (the same presented in Fig. 6). For *Gaia* sources we also display the proper motion vectors, in order to compare the velocity dispersion of stars with the radial velocity of the gas. The map clearly shows the secondary structure with velocities of $V > 17 \text{ km s}^{-1}$, while the gas in the main structure of the cloud has velocities ranging from less than 15 to $\sim 16.5 \text{ km s}^{-1}$, which supports the discussion based on Fig. 7. For our sample of YSOs, the proper motion velocity dispersion, measured in the plane of the sky, shows no remarkable trend that could indicate non-isotropic velocity patterns. This prevents us to address here a deeper integration of the stellar content with the gas kinematics for cloud sub-structures.

Mapping of the molecular line emission reveals the presence of dense cores, detected in the lines of ^{13}CO and CS. A sample of nine cores was investigated in more detail. The ^{12}CO and ^{13}CO line profiles are displayed in the right panel of Fig. 3. The observed line profiles were fitted by using a simple modeling of the ^{13}CO and C^{18}O lines, adopting a canonical relative abundance ratio $[\text{C}^{18}\text{O}]/[\text{C}^{16}\text{O}] = 8$. This allowed us to estimate the optical depths τ_{13} and τ_{18} of both isotopologues. The observed line profiles and optical depths were subsequently modeled with the radiative transfer code MADEX (Cernicharo 2012) in the large-velocity gradient approximation (Sobolev 1958, 1960), using the CO-H_2 collisional coefficients of Yang et al. (2010) and the line-width (FWHM) measured from a Gaussian fit to the line profiles. We could check that the results are essentially independent of $n(\text{H}_2)$ in the regime of densities $10^4\text{--}10^6 \text{ cm}^{-3}$, typical

of dark clouds and star-forming cores, namely, the ground state transitions are thermalized.

We adopted MADEX in this study to derive the kinetic temperature and the molecular gas column density in the cores. The main result is that these cores consist of cold gas, with temperatures in the range of 8–13 K. One of the most direct signs of protostellar activity is the signature of mass-loss phenomena (outflows) as broad wings in the CO rotational line profiles observed towards dense cores. This is illustrated in the CO lines profiles of cores 1, 3, 4, 5, 6, and 7 in Fig. 3. In the case of core 4, the outflow wings reach velocities as high as 20 km s^{-1} that is clear evidence for active, possibly massive, star formation in the core. Some of these cores (e.g., cores 6 and 7) are associated with IR (WISE) sources and we note that many of the IR sources coincide with the ^{13}CO cores identified in our map. We speculate that the absence of IR sources in the other cores which display bipolar outflow signatures indicates that the driving protostars might be at earlier stage of evolution, possibly Class 0.

Conversely, other dense cores detected in our observations appear to be in a quiescent stage, as illustrated by cores 2, 8, and 9 (Fig. 3). Based on our molecular gas content analysis (presented in Table 1), it appears that the cores in the northern part of the region ($n \geq 6$) tend to have lower gas column densities. More work is needed to confirm this trend (higher densities found in the southern part of the cloud), based on a very reduced sample, and to investigate whether it is related to the physical or chemical evolution (depletion, perhaps) of the region.

Despite the fact that all the dense cores (kinetic temperatures from 10 to 14 K) are found in the main structure, with most of the stellar members associated with it, there are 1 Class I and 8 Class II sources located in the direction of the secondary, smaller cloud structure. Since only two of these stars are *Gaia* sources, we cannot evaluate kinematic differences compared with the stars associated with the main structure.

Indeed, no trend is observed when comparing the spatial distribution of sources that have their proper motion vectors displayed in Fig. 8. The same can be said for the parallax distribution (see Fig. 4), where 9 Class III sources are also highlighted because they appear in the secondary structure, but without showing trends on ϖ . However, it is interesting to note that 2MASS07134800-1206336, found in the secondary structure, is the brightest star of the Class II objects ($G_{\text{Gaia}} = 13 \text{ mag}$), which appears in the red side of the color-magnitude diagram (see Fig. 6, right panel), with an age of $< 1 \text{ Myr}$. The parallax of this bright source indicates it is in the largest distance ($\varpi = 0.62 \pm 0.04$), as compared with the other members. Therefore, it is possible that the reddening still needs to be corrected for this source and its mass is expected to be greater than $2 M_{\odot}$.

6. Conclusions

In this study, we mapped molecular clouds with the IRAM-30 m to investigate the properties of cores and filaments to determine the spatial and kinematic distributions of gas in the cloud and their relation with the star formation activity. In the general context, we aim to search for and characterize the shock driven by the SN into the molecular cloud, which would be responsible for the gas compression and gravitational collapse.

Comparing the spatial distribution of the stellar population with the cores revealed by the ^{13}CO map, we verify that peaks of emission coincide with the position of YSOs (see Fig. 3). These results confirm that CMa harbors pre- and protostellar cores showing that star formation is still underway in cores distributed

along filaments, as suggested by Elia et al. (2013), based on a survey with *Herschel*.

We selected a sample of 89 sources, with 40 of them known to be confirmed members (*Gaia* EDR3) associated with CMA. The mean error-weighted parallax was converted to the distance of 1099^{+25}_{-24} pc, which is in excellent agreement with previous results for the CMA region (Clariá 1974; Tovmasyan et al. 1993; Shevchenko et al. 1999). Using the WISE colors, the sources were characterized according with the IR-excess. We are mainly interested here in Classes I and II that may have circumstellar disks. All of these disk-bearing stars are found around the filamentary structure of the cloud, despite several of them not being embedded, but more likely located in the cloud foreground. The color-magnitude diagram constructed with the G_{Gaia} photometry was used to verify whether the selected sources truly are pre-main sequence stars. The ages are less than 5 Myr for most of the sources, coinciding with ages estimated for the cluster found in the opposite side of the CMA shell. Moreover, as shown in Fig. 5 (right panel) and discussed below, the presence of embedded objects corresponding to protostellar phase (Class 0 and Class I sources) is confirmed in our sample. Since Class 0 and Class I stars have typical ages of 10^4 – 10^5 yr, they can be considered a direct evidence for sequential star formation in the region.

The kinematic analysis reveals the presence of two structures representing different parts of the cloud. A main structure, exhibiting $V = 15 \pm 1.2$ km s $^{-1}$, is formed from N to S in an extended stripe where most of the dense cores are found and YSOs are associated with. The secondary structure, seen at $V = 17.4 \pm 1.2$ km s $^{-1}$, grows from the south-west to the center of Fig. 3 (middle panel). The evidence of outflows is remarkable from the broad wings in the CO rotational line profiles observed in six dense cores, which are believed to be sites of protostellar activity, as indicated by their association with IR sources; this shows that a burst of star formation is currently ongoing. Follow-up observations, such as near-IR spectroscopy aimed at obtaining radial velocity of the members, are required to confirm the trends of stellar members following the cloud structure observed for this limited sample of objects associated with the studied region.

Despite the fact that these are partial results, our findings shed some light on the understanding of star formation in CMA. The age of the Class II population is consistent with the age and timescale of SNRs (Fernandes et al. 2019). The similarity of the young stellar population properties on eastern and western sides of the shell supports the scenario of a large-scale gravitational collapse of the shell, most likely induced by SN explosions.

We tentatively suggest that the presence of young protostellar population (with massive or intermediate-mass objects, as indicated by the strong outflow emission) could indicate that a second episode of star formation has recently taken place. The distribution of YSOs in the two gas layers at 15 and 17 km s $^{-1}$ suggests that local events on the eastern side (the region surveyed at IRAM) have contributed to driving the current star formation process. Our observations of the region altogether support the large-scale scenario of SNR that are shock-driven, but other processes on smaller scales appear to have influenced – and possibly induced – local star formation.

Acknowledgements. We acknowledge support from the Brazilian agencies: FAPESP grants 2014/18100-4 (JGH), 2017/19458-8 (AH), and 2014/22095-6 (EM); and CNPq grants 305590/2014-6 (JGH), and 150465/2019-0 (EM). B.L. and Md.S. acknowledge funding from the European Research Council (ERC) under the European Union’s Horizon2020 Research and Innovation program for the Project The Dawn of Organic Chemistry (DOC), grant agreement No 741002. Based on observations carried out under project number 043-18, 120-18, 034-20 with the IRAM-30 m telescope. IRAM is supported by INSU/CNRS

(France), MPG (Germany) and IGN (Spain). This work has made use of data from the European Space Agency (ESA) mission *Gaia* (<https://www.cosmos.esa.int/gaia>), processed by the *Gaia* Data Processing and Analysis Consortium (DPAC, <https://www.cosmos.esa.int/web/gaia/dpac/consortium>). Funding for the DPAC has been provided by national institutions, in particular the institutions participating in the *Gaia* Multilateral Agreement, his research has made use of “Aladin sky atlas” developed at CDS, Strasbourg Observatory, France (Boch & Fernique 2014; Bonnarel et al. 2000). This publication makes use of data products from the Wide-field Infrared Survey Explorer, which is a joint project of the University of California, Los Angeles, and the Jet Propulsion Laboratory/California Institute of Technology, funded by the National Aeronautics and Space Administration.

References

- Álvarez-Gutiérrez, R. H., Stutz, A. M., Law, C. Y., et al. 2021, *ApJ*, **908**, 86
- Boch, T., & Fernique, P. 2014, *ASPC* **485**, 277B
- Bonnarel, F., Fernique, P., Bienaymé, O., et al. 2000, *A&AS*, **143**, 33B
- Bressan, A., Marigo, P., Girardi, L., Salasnich, B. A., et al. 2012, *MNRAS*, **427**, 127B
- Cardelli, J. A., Clayton, G. C., & Mathis, J. S. 1989 *ApJ*, **345**, 245
- Cernicharo, J. 2012, *EAS Pub. Ser.*, **58**, 251
- Clariá, J. J. 1974, *A&A*, **37**, 229
- Cutri, R. M., Wright, E. L., Conrow, T., et al. 2013, The AllWISE Data Release Products
- Dale, J. E., Haworth, T. J., & Bressert, E. 2015, *MNRAS*, **450**, 1199
- Desai, K. M., Chu, Y.-H., & Gruendl, R. A., et al. 2010, *AJ*, **140**, 584
- Dias, W. S., Monteiro, H., Caetano T. C., et al. 2014, *A&A*, **564**, A79
- Dobashi, K. 2011, *PASJ*, **63S**, 1D
- Elia, D., Molinari, S., Fukui, Y., et al. 2013, *ApJ*, **772**, 45
- Elmegreen, B. G., & Lada, C. J. 1977, *ApJ*, **214**, 725
- Fernandes, B., Montmerle, T., Gregorio-Hetem, J., Santos-Silva, T. 2019, *A&A*, **628**, A44
- Fischer, W. J., Padgett, D. L., Stapelfeldt, K. L., & Sewilo, M. 2016, *ApJ*, **827**, 96
- Gaia Collaboration (Prusti, T., et al.) 2016, *A&A*, **595**, A1
- Gaia Collaboration (Brown, A. G. A., et al.) 2020, *A&A*, **595**, A2
- Gregorio-Hetem J. 2008, in *Handbook of Star Forming Regions*, ed. B. Reipurth, (USA: ASP Books), 2, 1
- Gregorio-Hetem J., Montmerle T., Rodrigues C. V., et al. 2009, *A&A*, **506**, 711
- Gregorio-Hetem J., Navarete, F., Hetem, A., et al. 2021, *AJ* **161**, 133
- Griffin, M. J., Abergel, A., Abreu, A., et al. 2010, *A&A*, **518**, L3
- Helou, G., & Walker, D. W. 1988 *Infrared Astronomical Satellite (IRAS) Catalogues and Atlases* (USA: NASA) 7, 1
- Hensler, G. 2011, *IAU Symp.*, **270**, 309
- Herbst, W., & Assousa, G. E. 1977, *ApJ*, **217**, 473
- Hetem, A., & Gregorio-Hetem, J. 2019, *MNRAS*, **490**, 2521
- Kang, J.-h., Koo, B.-C., & Salter, C. 2012, *AJ*, **143**, 75
- Kim, B. G., Kawamura, A., Yonekura, Y., & Fukui, Y. 2004. *PASJ*, **56**, 313
- Kirsanova, M. S., Wiebe, D. S., Sobolev, et al. 2014, *MNRAS*, **437**, 1593
- Koenig, X. P., & Leisawitz, D. T. 2014, *ApJ*, **791**, 131
- Lefloch, B., Cernicharo, J., & Pardo, J. 2008, *A&A*, **489**, 157
- Marigo, P., Girardi, L., Bressan, A., et al. 2017, *ApJ*, **835**, 77M
- Molinari, S., Swinyard, B., Bally, J., et al. 2010, *PASP*, **122**, 314
- Navarete, F., Galli, P. A. B., Damineli, A. 2019, *MNRAS*, **487**, 2771
- Onishi, T., Nishimura, A., Ota, Y., et al. 2013, *PASJ*, **65**, 78
- Pettersson, B., & Reipurth, B. 2019, *A&A* **630**, A90
- Pilbratt, G. L., Riedinger, J. R., Passvogel, T., et al. 2010, *A&A*, **518**, L1
- Poglitsch, A., Waelkens, C., Geis, N., et al. 2010, *A&A*, **518**, L2
- Rebull, L. M., Padgett, D. L., McCabe, C.-E., et al. 2010, *ApJS* **186**, 259
- Santos-Silva, T., Gregorio-Hetem, J., Montmerle, T. Fernandes, B., & Stelzer, B. 2018, *A&A*, **609**, A127
- Santos-Silva, T., Perottoni, H. D., Almeida-Fernandes, F., et al. 2021, *MNRAS*, **508**, 1033
- Shevchenko, V. S., Ezhkova, O. V., Ibrahimov, M. A., van den Ancker, M. E., & Tjin A Dje, H. R. E. 1999, *MNRAS*, **310**, 210
- Sobolev, V.V. 1958 *Theoretical Astrophysics*, ed. Ambartsumyan (London: Pergamon Press Ltd.)
- Sobolev, V.V. 1960 *Moving Envelopes of Stars* (Cambridge: Harvard University Press)
- Stutz, A. M., & Gould, A. 2016, *A&A*, **590**, A2
- Tovmasyan, H. M., Oganesyan, R. Kh., Epremyan, R. A., & Yuzgenen, D. 1993, *AZh*, **70**, 451
- Vaupré, S., Hily-Blant, P., Ceccarelli, C., et al. 2014, *A&A*, **568**, A50
- Wright, E. L., Eisenhardt, P. R. M., Mainzer, A. K., et al. 2010, *AJ*, **140**, 1868
- Xu, J.-L., Wang, J.-J., & Miller, M. 2011, *ApJ*, **727**, 81
- Yang, et al. 2010, *ApJ*, **718**, 1062

Appendix A: Additional tables

Table A.1. Membership probability, parallax, proper motion, and *Gaia* EDR3 photometry.

<i>Gaia</i> EDR3	P %	ϖ mas	μ_α mas/yr	μ_δ mas/yr	G mag	G_{BP} mag	G_{RP} mag
3045239083971370112	87	0.77 ± 0.17	-3.21 ± 0.16	0.91 ± 0.15	18.65	20.43	17.24
3045208886056506112	13	1.69 ± 1.10	-2.52 ± 0.86	0.97 ± 1.06	20.33	21.63	18.78
3045225516172964864 ^a	95	0.66 ± 0.02	-3.32 ± 0.02	0.74 ± 0.02	13.80	14.77	12.74
3045229291445342592 ^b	92	1.31 ± 0.19	-3.26 ± 0.18	0.98 ± 0.16	18.80	20.42	17.43
3045227749555916032 ^c	91	0.61 ± 0.14	-3.11 ± 0.16	0.88 ± 0.13	17.93	19.59	16.63
3045131301773079168	90	0.79 ± 0.10	-3.02 ± 0.08	1.04 ± 0.09	17.44	19.06	16.22
3045208950479742208	83	1.12 ± 0.26	-3.28 ± 0.20	1.11 ± 0.18	18.89	20.72	17.57
3045237434703416320	82	1.63 ± 0.39	-3.52 ± 0.34	1.09 ± 0.33	19.89	21.26	18.52
3045235785435946624	79	0.72 ± 0.32	-3.13 ± 0.26	1.22 ± 0.24	19.03	20.96	17.65
3045117141257872000	78	1.00 ± 0.30	-3.49 ± 0.28	0.90 ± 0.29	19.01	20.52	17.75
3045215998525392384 ^d	65	0.97 ± 0.11	-2.93 ± 0.11	0.43 ± 0.10	17.29	19.13	15.91
3045116114758900736	65	0.57 ± 0.52	-4.38 ± 0.53	1.48 ± 0.54	19.99	21.22	18.57
3045114804796665984	63	1.02 ± 0.51	-3.17 ± 0.44	2.00 ± 0.48	19.85	21.54	18.39
3045214070080777600	27	0.92 ± 1.18	-2.78 ± 0.90	0.44 ± 1.00	20.66	21.37	19.22
3045234170527254656	21	0.45 ± 0.10	-3.00 ± 0.10	0.87 ± 0.09	17.39	19.19	16.07
3045235785436006400	21	1.47 ± 0.80	-3.48 ± 0.62	0.54 ± 0.63	20.26	21.51	18.81
3045118416872687744	92	0.96 ± 0.03	-3.69 ± 0.03	0.99 ± 0.03	12.85	12.97	12.63
3045226821842999552	97	0.80 ± 0.05	-3.51 ± 0.06	1.03 ± 0.06	16.32	17.39	15.29
3045213352825581312	97	0.89 ± 0.02	-3.28 ± 0.02	0.99 ± 0.02	14.03	14.49	13.40
3045228368031224448	96	0.84 ± 0.05	-3.23 ± 0.05	1.15 ± 0.05	15.86	16.64	14.99
3045215758007221632	94	0.79 ± 0.04	-3.19 ± 0.04	0.94 ± 0.04	15.85	16.76	14.87
3045232555619709056	93	1.17 ± 0.02	-3.60 ± 0.02	0.83 ± 0.02	14.50	14.87	13.97
3045114809098665984	92	0.76 ± 0.02	-3.22 ± 0.01	1.01 ± 0.01	12.60	12.99	12.02
3045229291444432384	90	0.50 ± 0.18	-4.08 ± 0.16	1.06 ± 0.14	18.59	20.14	17.32
3045114701716408832	90	0.90 ± 0.21	-3.53 ± 0.18	1.11 ± 0.20	18.70	20.30	17.46
3045114843459884288	90	0.87 ± 0.41	-3.71 ± 0.33	1.46 ± 0.36	19.60	20.97	18.36
3045209156636885760	85	0.72 ± 0.13	-2.71 ± 0.11	0.94 ± 0.09	17.68	19.11	16.52
3045114396781820672	84	0.91 ± 0.03	-3.11 ± 0.02	0.96 ± 0.02	14.53	14.88	14.02
3045118382511875712	82	0.88 ± 0.05	-3.90 ± 0.04	0.97 ± 0.04	15.81	16.43	15.05
3045227509039371648	80	0.44 ± 0.37	-2.95 ± 0.36	0.94 ± 0.30	19.39	20.99	18.11
3045233242814458752	79	0.67 ± 0.19	-2.92 ± 0.20	1.19 ± 0.22	18.63	20.13	17.47
3045229879859736704	70	0.51 ± 0.10	-4.33 ± 0.09	1.11 ± 0.10	17.53	18.91	16.38
3045207885326442496	70	1.27 ± 0.31	-3.06 ± 0.24	0.87 ± 0.23	19.34	20.71	18.19
3045228952146750208	70	0.55 ± 0.13	-2.88 ± 0.14	1.02 ± 0.12	18.11	20.01	16.81
3045130678995758848	69	1.37 ± 0.28	-3.63 ± 0.33	1.67 ± 0.34	19.26	20.84	17.97
3045130472837058176	66	1.56 ± 0.59	-2.26 ± 0.70	0.83 ± 0.72	20.20	21.74	18.88
3045420954362862336	64	1.38 ± 0.03	-3.52 ± 0.03	1.56 ± 0.03	15.32	15.85	14.62
3045212936208209024	64	0.60 ± 0.39	-2.34 ± 0.30	1.02 ± 0.33	19.33	20.77	18.11
3045233693790633472	62	1.25 ± 0.19	-2.80 ± 0.17	1.70 ± 0.16	18.58	19.99	17.43
3045233281473783936	59	0.92 ± 0.01	-3.01 ± 0.02	1.00 ± 0.02	13.50	13.92	12.89
3045213623404184448	58	1.37 ± 0.40	-2.63 ± 0.36	0.66 ± 0.31	19.46	21.21	18.14
3045233998728534272	56	0.56 ± 0.37	-2.45 ± 0.29	1.47 ± 0.27	19.58	20.97	18.31
3045233487625692160	53	0.81 ± 0.57	-3.79 ± 0.78	1.65 ± 0.95	20.07	21.24	18.75
3045225202636012800	50	1.06 ± 0.58	-3.88 ± 0.61	0.45 ± 0.64	20.04	21.43	18.73

Notes: The objects are distinguished by: Class I (top); Class II (middle); Class III (bottom), according with Table A.2. Stars identified as $H\alpha$ emitters are indicated by (a) ID 381; (b) ID 387; (c) ID 390; and (d) ID 392, where the ID numbers are given by Pettersson & Reipurth (2014).

Table A.2. Infrared photometry for stellar populations.

<i>Gaia</i> EDR3	2MASS	J mag	H mag	K mag	W1 mag	W2 mag	W3 mag	W4 mag	Class
3045239083971370112	07141347-1152298	14.44	12.88	11.82	10.97	9.82	6.99	4.61	I
3045208886056506112	07141796-1214324	15.55	14.05	13.13	11.60	10.46	7.88	5.63	I
3045225516172964864	07134800-1206336	10.79	9.62	8.65	7.62	7.00	4.55	2.66	II
3045229291445342592	07141244-1157517	15.24	13.89	12.94	11.40	10.61	8.49	6.41	II
3045227749555916032	07141939-1203191	13.39	12.11	11.29	10.32	9.66	7.51	5.74	II
3045131301773079168	07133622-1210420	14.09	12.89	12.24	12.04	11.40	8.67	6.45	II
3045208950479742208	07142387-1214061	15.06	13.94	13.45	12.66	11.91	8.71	5.69	II
3045237434703416320	07143525-1152374	15.79	14.37	13.56	12.79	12.13	10.54	5.78	II
3045235785435946624	07142515-1154273	15.02	13.74	12.92	11.77	11.20	9.96	8.38	II
3045117141257872000	07133088-1216043	15.21	14.02	13.45	12.73	11.98	9.56	7.42	II
3045215998525392384	07142409-1203377	13.20	11.99	11.32	10.40	9.57	7.20	4.77	II
3045116114758900736	07133958-1217599	15.54	14.04	13.27	12.56	12.03	9.86	7.85	II
3045114804796665984	07140707-1217153	15.73	14.87	14.32	13.98	13.48	10.03	7.68	II
3045214070080777600	07142847-1209146	15.65	14.24	13.20	12.39	11.49	9.07	6.47	II
3045234170527254656	07142755-1158460	13.72	12.58	12.07	11.39	10.69	8.47	6.48	II
3045235785436006400	07142353-1154135	15.57	14.19	13.32	12.39	11.71	9.72	7.41	II
3045118416872687744	07133684-1216484	12.36	12.30	12.23	12.20	12.22	12.39	9.09	III
3045226821842999552	07135758-1203138	13.71	12.96	12.79	12.76	12.68	12.27	9.14	III
3045213352825581312	07140300-1208579	12.61	12.20	12.07	12.04	12.05	11.67	8.50	III
3045228368031224448	07135653-1202357	13.74	13.14	12.92	12.84	12.88	12.41	9.07	III
3045215758007221632	07143221-1204404	13.33	12.83	12.50	12.47	12.39	12.00	8.71	III
3045232555619709056	07140255-1156164	13.36	13.02	12.93	12.95	12.98	11.62	8.90	III
3045114809098665984	07141006-1217243	11.28	11.12	11.00	10.87	10.87	9.43	7.40	III
3045229291444432384	07141365-1158183	15.07	14.21	13.78	13.53	13.47	12.37	9.00	III
3045114701716408832	07141366-1217431	15.13	14.28	13.94	13.62	13.63	10.67	8.42	III
3045114843459884288	07140167-1217317	16.24	15.64	15.33	15.60	15.44	12.60	9.21	III
3045209156636885760	07143327-1213273	14.53	13.68	13.34	13.10	13.05	12.12	9.17	III
3045114396781820672	07140309-1218168	13.47	13.14	13.07	13.03	13.08	11.97	8.84	III
3045118382511875712	07134177-1216279	14.08	13.51	13.40	13.28	13.31	12.52	8.74	III
3045227509039371648	07140828-1203310	15.77	14.66	14.25	14.07	13.98	12.34	8.96	III
3045233242814458752	07134763-1156272	15.44	14.65	14.34	14.28	14.44	11.83	9.05	III
3045229879859736704	07132666-1202354	14.46	13.69	13.38	13.20	13.19	11.89	8.18	III
3045207885326442496	07142893-1216095	16.30	15.84	15.17	15.37	16.12	12.35	9.05	III
3045228952146750208	07141111-1159429	14.36	13.45	12.94	12.70	12.59	11.88	9.09	III
3045130678995758848	07133413-1212033	15.80	14.49	13.90	13.19	12.72	11.19	8.08	III
3045130472837058176	07133056-1214195	16.44	15.26	15.36	14.78	14.65	12.48	8.72	III
3045420954362862336	07133375-1153320	13.75	13.22	13.03	13.10	13.17	12.67	8.95	III
3045212936208209024	07140301-1211153	16.01	15.16	14.53	14.51	14.40	12.69	9.17	III
3045233693790633472	07135366-1153340	15.90	15.21	14.91	14.88	15.07	12.38	9.05	III
3045233281473783936	07135236-1156044	12.15	11.76	11.70	11.64	11.66	12.41	8.99	III
3045213623404184448	07141889-1208085	15.35	14.20	13.62	13.51	13.29	12.72	8.99	III
3045233998728534272	07143643-1159120	16.21	15.47	14.97	14.79	14.79	12.22	8.91	III
3045233487625692160	07135485-1154240	16.80	15.88	15.64	15.64	15.76	11.70	8.68	III
3045225202636012800	07135247-1208309	16.23	15.27	14.69	14.68	14.51	12.05	8.92	III